

Prospects for thermalization of microwave-shielded ultracold molecules

Reuben R. W. Wang  and John L. Bohn *JILA, NIST, and Department of Physics, University of Colorado, Boulder, Colorado 80309, USA* (Received 26 October 2023; revised 8 February 2024; accepted 16 April 2024; published 6 May 2024)

Toward more efficient schemes for achieving deeply degenerate molecular Fermi gases, we study anisotropic thermalization in dilute gases of microwave shielded polar molecular fermions. For collision energies above the threshold regime, we find that thermalization is suppressed due to a strong preference for forward scattering and a reduction in total cross section with energy, significantly reducing the efficiency of evaporative cooling. We perform close-coupling calculations on the effective potential energy surface derived by Deng *et al.* [*Phys. Rev. Lett.* **130**, 183001 (2023)] to obtain accurate two-body elastic differential cross sections across a range of collision energies. We use Gaussian process regression to obtain a global representation of the differential cross section over a wide range of collision angles and energies. The route to equilibrium is then analyzed with cross-dimensional rethermalization experiments, quantified by a measure of collisional efficiency toward achieving thermalization.

DOI: [10.1103/PhysRevResearch.6.L022033](https://doi.org/10.1103/PhysRevResearch.6.L022033)

The ever-growing interest in quantum control of polar molecules motivates the cooling of molecular gases to unprecedented cold temperatures [1–5]. In bulk gases, reaching such temperatures can be accomplished through evaporative cooling [6], a process which throws away energetic molecules and leverages collisions to rethermalize the remaining, less energetic distribution. Understanding and controlling two-body scattering for thermalization is, therefore, of great importance for ultracold experiments. To this end, the exciting advent of collisional shielding with external fields has permitted a large suppression of two-body losses between molecules [7–11]. Thermalization relies instead on the elastic cross section, which is generally dependent on the field-induced dipole-dipole interaction and their energy of approach. Of particular interest to this Letter is collisional shielding with microwave fields [12–15], recently achieved at several labs around the world [16–19].

In analogous gases of magnetic atoms with comparatively small dipole moments, dipolar scattering remains close to threshold [20] at the ultracold but nondegenerate temperatures of $T \sim 100$ nK [21–24]. For dipoles, threshold scattering occurs when the collision energy is much lower than the characteristic dipole energy, in which case the scattering cross section becomes energy independent [25] with a universal analytic form [26]. Numerical studies of thermalization are made much simpler at universality, since collisions can be sampled regardless of collision energy [27,28]. However, this convenience is lost with the polar molecular gases of interest here. Take, for instance, a gas of fermionic $^{23}\text{Na}^{40}\text{K}$, as we will concern ourselves with in this Letter. This species has a large intrinsic dipole moment of $d = 2.72$ D, so even ultracold

temperatures have the majority of collisions occurring away from threshold with an energy-dependent cross section.

In this Letter, we find that nonthreshold collisions can dramatically reduce thermalization and thus, the efficiency of the cooling process. Ignoring all one- and two-body losses for a focused study on elastic collisions, the decrease in gas total energy $E = 3Nk_B T$ along with the number of molecules N , approximately follows the coupled rate equations [18,29]

$$\frac{dN}{dt} = -\nu(\kappa)\gamma_{\text{th}}N, \quad (1a)$$

$$\frac{dE}{dt} = -\frac{1}{3}\lambda(\kappa)\gamma_{\text{th}}E, \quad (1b)$$

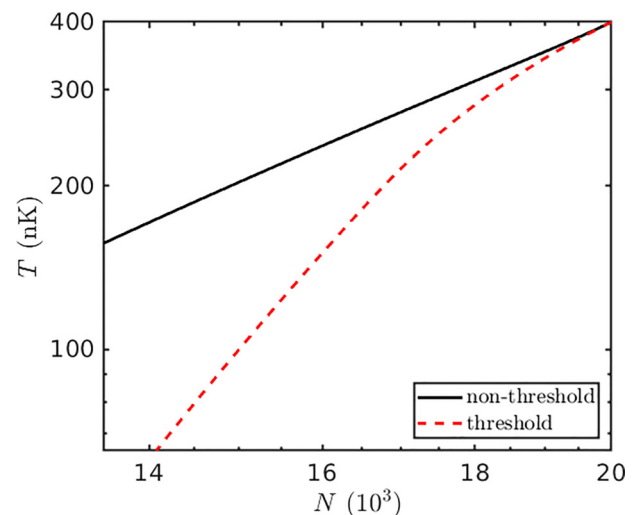


FIG. 1. A log-log plot of T vs N during a forced evaporation protocol. The plot compares the evaporation trajectory for microwave-shielded $^{23}\text{Na}^{40}\text{K}$ when scattering is realistic and non-threshold (solid black curve) to the artificial case of threshold scattering (dashed red curve). Both one- and two-body losses are assumed negligible and ignored here.

Published by the American Physical Society under the terms of the [Creative Commons Attribution 4.0 International license](https://creativecommons.org/licenses/by/4.0/). Further distribution of this work must maintain attribution to the author(s) and the published article's title, journal citation, and DOI.

where $\nu(\kappa) = (2 + 2\kappa + \kappa^2)/(2e^\kappa)$ and $\lambda(\kappa) = (6 + 6\kappa + 3\kappa^2 + \kappa^3)/(2e^\kappa)$ are functions of the energetic truncation parameter $\kappa = U/(k_B T)$ [30].

By continuously lowering the energetic depth of the confining potential $U(t) = U_0 \exp(-t/\tau)$ over a time interval τ , highly energetic molecules are forced to evaporate away, lowering the number of molecules along with the gas temperature, as shown in Fig. 1. For the plot, Eq. (1) is solved by taking evaporation to start at an initial temperature of $T_0 = 400$ nK and molecule number $N_0 = 20\,000$, lowering the trap depth from $U_0/k_B = 4$ μ K over $\tau = 0.5$ s. The gas is assumed to be harmonically confined with trapping frequencies $(\omega_x, \omega_y, \omega_z) = 2\pi \times (160, 160, 40)$ Hz, although the specific trap geometry does not affect thermalization dynamics in the dilute regime [28]. The evaporation efficiency, defined as the slope of T vs N on a log-log scale, is governed by the thermalization rate γ_{th} . The figure shows efficient cooling for the low-energy threshold cross sections (dashed red curve), and significantly less efficient cooling for the realistic cross sections (solid black curve). The remainder of this Letter provides the microscopic mechanisms that lead to this dramatic difference, and efficient theoretical tools we employ to obtain these conclusions.

Shielded collisions. Central to this Letter are collisions that occur between molecules shielded by circularly polarized microwaves [15]. The resulting potential energy surface between two such molecules is conveniently described by a single effective potential [31],

$$V_{\text{eff}}(\mathbf{r}) = \frac{C_6}{r^6} [1 - (\hat{\mathbf{r}} \cdot \hat{\mathbf{E}})^4] + \frac{\bar{d}^2}{4\pi\epsilon_0} \frac{3(\hat{\mathbf{r}} \cdot \hat{\mathbf{E}})^2 - 1}{r^3}, \quad (2)$$

where $\mathbf{r} = (r, \theta, \phi)$ is the relative position between the two colliding molecules, $\hat{\mathbf{E}}$ is the axis along which the dipoles are effectively aligned, $\bar{d} = d_0/\sqrt{12(1 + (\Delta/\Omega)^2)}$ is the effective molecular dipole moment, and $C_6 = d_0^4(1 + (\Delta/\Omega)^2)^{-3/2}/(128\pi^2\epsilon_0^2\hbar\Omega)$. Here Δ and Ω are the detuning and Rabi frequency, respectively, of the microwaves. A $y = 0$ slice of the effective microwave shielding interaction potential with $\hat{\mathbf{E}} = \hat{\mathbf{z}}$ is plotted in the inset of Fig. 2. Notably, the long-range $1/r^3$ tail of $V_{\text{eff}}(\mathbf{r})$ is almost identical to that of point dipole particles, modified only by an overall minus sign. As a result, the close-to-threshold elastic cross sections for microwave shielded molecules are identical to those for point dipoles.

It is natural to introduce units based on the reduced mass μ , dipole length, and dipole energy,

$$a_d = \frac{\mu \bar{d}^2}{4\pi\epsilon_0 \hbar^2} \quad \text{and} \quad E_{\text{dd}} = \frac{\hbar^2}{\mu a_d^2}, \quad (3)$$

respectively. Threshold scattering is then expected to occur for collision energies $E \ll E_{\text{dd}}$. With the microwave parameters $\Delta = 2\pi \times 15$ MHz and $\Omega = 2\pi \times 9.5$ MHz, which will be assumed in what follows, the molecules are not expected to see the recently observed field-linked resonances at zero microwave ellipticity [31,32]. Then, considering only nonresonant scattering, the molecules see a dipole length of $a_d \approx 3900a_0$, corresponding to a dipole energy of

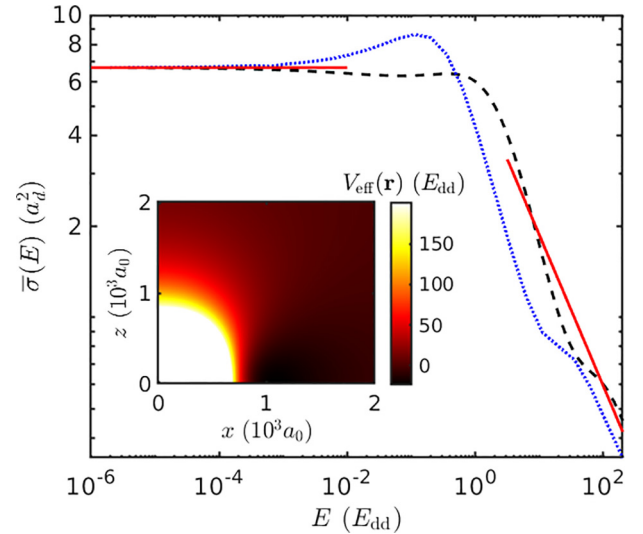


FIG. 2. Energy dependence of the angular averaged total cross section $\bar{\sigma}$ between microwave-shielded $^{23}\text{Na } ^{40}\text{K}$ (black dashed line). The energy dependence clearly differs from the total cross section between fermionic point dipoles (dotted blue curve). For comparison, we plot the low-energy Born and high-energy Eikonal approximations with solid red lines. The inset shows a $y = 0$ slice of the effective microwave shielding interaction potential, with Rabi frequency $\Omega = 2\pi \times 15$ MHz and microwave detuning $\Delta = 2\pi \times 9.5$ MHz. The shielding core is depicted as a white patch surrounding the coordinate origin which saturates the color bar at $V_{\text{eff}} > 200E_{\text{dd}}$. Coordinate axes are plotted in units of 10^3 Bohr radii a_0 .

$E_{\text{dd}}/k_B \approx 360$ nK. Therefore, temperatures comparable to E_{dd}/k_B are insufficient to keep molecular scattering in the threshold regime [25]. Moreover, since the dipole energy scales as $E_{\text{dd}} \sim d^{-4}$, larger dipoles require much lower temperatures to achieve universal dipolar threshold scattering, as alluded to earlier. Away from threshold, the integral cross section $\bar{\sigma}$ in the presence of microwave shielding (dashed black curve) develops a nontrivial energy dependence that clearly differs from that of plain point dipoles (dotted blue curve), as illustrated in Fig. 2. The plotted cross sections were obtained from close-coupling calculations logarithmically spaced in energy, with a universal loss short-range boundary condition [33] (see Supplemental Material [34] for further details).

Away from threshold at $E \approx E_{\text{dd}}$, the microwave-shielded integral cross section does not deviate much from its value at threshold (solid red line in Fig. 2). But the differential cross section could still have its anisotropy changed substantially, which is what ultimately affects thermalization [26]. For a study of both nonthreshold differential scattering and its implications to thermalization in nondegenerate Fermi gases, we take its nonequilibrium evolution as governed by the Boltzmann transport equation [35]. Formulated in this way, numerical solutions treat the molecular positions and momenta as classical variables, while collisions can be efficiently accounted for means of Monte Carlo sampling [27,36]. But on the fly, close-coupling calculations would be too expensive for such sampling over a broad range of collision energies and angles. Instead, we propose the following.

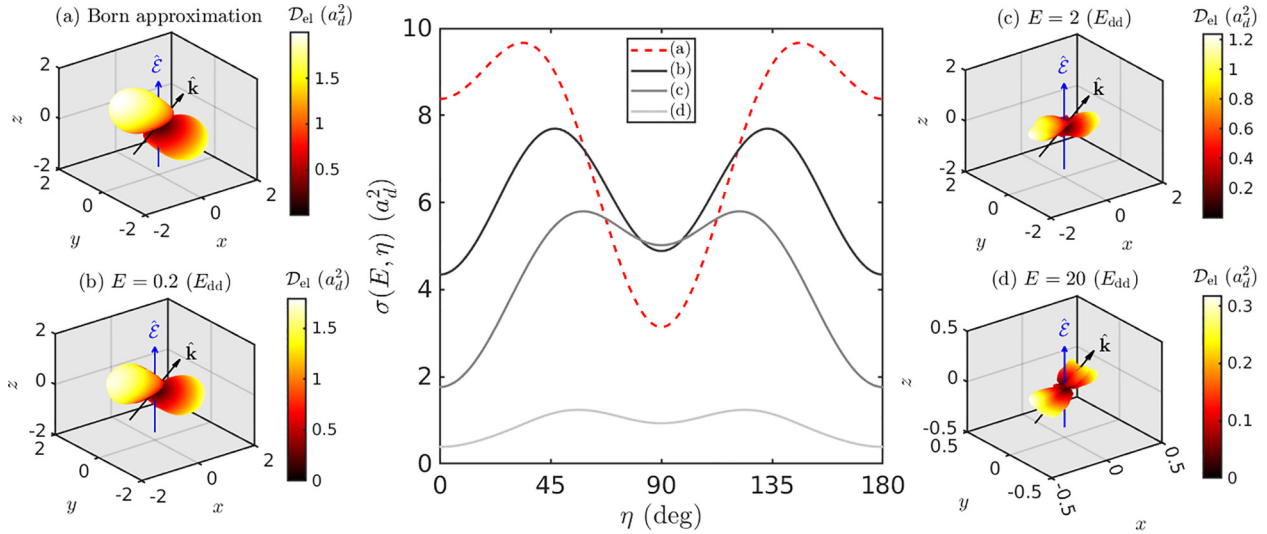


FIG. 3. The central plot shows the total cross section as a function of the incident collision angle, obtained from (a) the Born approximation (red dashed curve) and from GP interpolation (solid curves) for three different collision energies: (b) $E = 0.2E_{\text{dd}}$ (black), (c) $E = 2E_{\text{dd}}$ (gray), and (d) $E = 20E_{\text{dd}}$ (light gray). In alphabetical correspondence are angular plots of the differential cross section (in units of a_d^2) in subplots with the respective collision energies, assuming dipoles pointing along $\hat{\mathcal{E}} = \hat{z}$ and incident collision angle $\eta = 45^\circ$ lying in the x, z plane. (d) uses a smaller domain for clarity of presentation.

Gaussian process fitting. At a given collision energy, the elastic differential cross section \mathcal{D}_{el} is a function of the dipole alignment axis $\hat{\mathcal{E}}$, and the relative ingoing and outgoing momentum vectors $\hbar\mathbf{k}$ and $\hbar\mathbf{k}'$, respectively. Collectively, we refer to this set of parameters as β . By first performing close-coupling calculations at several well-chosen collision energies $E = \hbar^2 k^2 / (2\mu)$ [37], we can use the resultant scattering data to infer an M -dimensional continuous hypersurface that approximates \mathcal{D}_{el} with a Gaussian process (GP) model [38–40].

GP regression is a machine-learning technique used to interpolate discrete data points, stitching them together to form a continuous global surface. To do so, a GP assumes that $\mathcal{D}_{\text{el}}(\beta)$ evaluated at any two nearby points in its coordinate space, β_i and β_j , are Gaussian distributed with a covariance given in terms of a function $K(\beta_i, \beta_j)$, called the kernel. A parameterized functional form for the kernel is chosen prior to the surface fitting process, reducing the task of combing through an infinite space of possible functions that best match the data, to a minimization over the kernel parameters. This minimization step is referred to as *training* the GP model.

Several symmetries in the differential cross section help to reduce the computational load of training slightly. Rotated into the frame where $\hat{\mathcal{E}}$ points along the z axis, which we refer to as the dipole frame, the unique hypersurface regions effectively live in an $M = 4$ dimensional space, with coordinates $\beta = (E, \eta, \theta_s, \phi_s)$. As defined, $\eta = \cos^{-1} \hat{\mathbf{k}} \cdot \hat{\mathcal{E}}$ is the angle between the dipole and incident relative momentum directions, where it is convenient to select $\hat{\mathbf{k}}$ to lie in its x, z plane. The scattering angles, labeled with a subscript s , are defined in the dipole-frame such that $\mathbf{k}' = (k', \theta_s, \phi_s)$ [41]. More details of the appropriate frame transformations are provided in Supplemental Material [34].

To perform the interpolation with GP regression, we utilize the Matérn- $\frac{5}{2}$ kernel [42], which is better able to capture the sharp jumps in a nonsmooth function, over higher-order

differentiable kernels such as the radial basis function [43]. This kernel is typically not ideal for periodic input data, so we make the periodicity of the angles (η, θ_s, ϕ_s) explicitly known to the GP model by training it with the cosine of these angles instead of the angles themselves. Furthermore, $\log_{10}(E/E_{\text{dd}})$ is fed into the GP model in place of E to reduce the disparity in fitting domains between each coordinate of β . The GP model is trained over the range $\log_{10}(E/E_{\text{dd}}) = -6$ to 2, corresponding to collision energies of $E/k_B \approx 0.36$ pK to 36 μ K. After training on $\sim 10\,000$ samples of $\mathcal{D}_{\text{el}}(E, \eta, \theta_s, \phi_s)$, the resulting GP fit obtains a mean-squared error of $\approx 0.5\%$ against the close-coupling calculations [44], which we take as an accurate representation of the actual cross section.

In Fig. 3, we plot the total cross section $\sigma(E, \eta) = \int \mathcal{D}_{\text{el}}(E, \eta, \Omega_s) d\Omega_s$ at various collision energies. There is a marked variation in the η dependence, indicating a higher tendency for side-to-side collisions ($\eta = 90^\circ$) over head-to-tail ones ($\eta = 0^\circ$) at higher energies. To highlight the dominant anisotropic scattering process, Fig. 3 also provides plots of the differential cross section at $\eta = 45^\circ$, the approximate angle at which σ is maximal. As energy increases from Figs. 3(a) to 3(d), the scattered angle dependence of \mathcal{D}_{el} becomes biased toward forward scattering, reducing the effectiveness of collisions for thermalization as discussed below. Alphabetic labels in Fig. 3 consistently correspond to the collision energies: (b) $E = 0.2E_{\text{dd}}$, (c) $E = 2E_{\text{dd}}$, and (d) $E = 20E_{\text{dd}}$. The Born approximated cross sections at threshold [26] are labeled with (a).

Collisional thermalization. Fast and easy access to the accurate differential cross section via its GP model now permits accurate theoretical investigations of nondegenerate gas dynamics. More specifically, we are concerned here with a gas' route to thermal equilibrium. A common experiment for such analysis is cross-dimensional rethermalization [45], in which

a harmonically trapped gas is excited along one axis, then left alone to re-equilibrate from collisions.

We present results in terms of the temperatures along each axis i , defined in the presence of a harmonic trap as $\mathcal{T}_i = (\langle p_i^2 \rangle / m + m\omega_i^2 \langle q_i^2 \rangle) / 2$, where $\langle \dots \rangle = \int d^3q d^3p f(\mathbf{q}, \mathbf{p}) (\dots)$ denotes a phase space average over the phase space distribution f in molecular positions \mathbf{q} and momenta \mathbf{p} , while ω_i are the harmonic trapping frequencies. The axes for \mathcal{T}_i are those in a laboratory frame, defined such that $\hat{\mathcal{E}}$ lies in its x, z -plane with angle Θ from \hat{z} . As is usual in cross-dimensional rethermalization, we consider an excitation of axis i , then proceed to measure the thermalization rate along axis j . This is modeled by taking axis i to have an initial out-of-equilibrium temperature $\mathcal{T}_i = T_0 + \delta_i / k_B$, with a perturbation in energy δ_i , while the other two axes are simply at initial temperature T_0 .

In the case of a dilute gas, the relaxation of \mathcal{T}_j follows an exponential decay in time, whose rate γ_{ij} is related to the standard collision rate γ_{coll} by a proportionality factor $\varepsilon_{ij} = \gamma_{ij} / \gamma_{\text{coll}}$. As defined, the quantity ε_{ij} is the inverse of the so-called number of collisions per rethermalization [45,46], a measure of thermalization common to the literature [10,17,18]. We opt to utilize its inverse instead, as it is the more natural definition to discuss efficiency of evaporative cooling. Usually defined as $\gamma_{\text{coll}} = \langle n \rangle \langle \bar{\sigma} v_r \rangle$ with phase space averaged number density $\langle n \rangle$ and two-body elastic rate $\langle \bar{\sigma} v_r \rangle$, ε_{ij} represents the efficiency of each nonthreshold collision toward thermalization of the gas. This collisional efficiency is formally cast in terms of the integral

$$\varepsilon_{ij} \approx \alpha_{ij} \frac{\pi^2}{64} \int \frac{d^3\kappa}{(2\pi)^3} \frac{e^{-\kappa^2/4}}{\sqrt{\pi}} \int d^2\Omega' \frac{\mathcal{D}'_{\text{el}} \kappa}{\langle \sigma \kappa \rangle} \Delta \kappa_i^2 \Delta \kappa_j^2, \quad (4)$$

where $\Delta \kappa_i^2 = \kappa_i'^2 - \kappa_i^2$ is the collisional change in adimensional relative momenta $\kappa = \mathbf{p}_r (mk_B T_0)^{-1/2}$, $\alpha_{ij} = 3/2$ if $i = j$, and $\alpha_{ij} = -3$ otherwise (see Supplemental Material [34]). The integral above has been evaluated analytically in the threshold scattering regime [28], both for identical dipolar fermions and bosons.

Evidently, from Eq. (4), ε_{ij} is symmetric in its indices which leaves only six unique configurations of i and j . We compute Eq. (4) with Monte Carlo integration [47] and plot ε_{xz} versus Θ as representative example in Fig. 4. The solid curves are ε_{xz} at the temperatures $T = 10$ nK (black), $T = 100$ nK (dark gray), $T = 400$ nK (gray), and $T = 1$ μ K (light gray). We find a consistent decrease in the collisional efficiency with increasing temperature, which can be intuited by looking at the differential cross section around $\eta = 45^\circ$, around which the total cross section is maximal. As evidenced from the subplots of \mathcal{D}_{el} in Fig. 3, forward scattering is favored at higher collision energies, limiting momentum transfer between axes and, therefore, also the efficiency of collisions toward rethermalization. Preferential forward scattering is what ultimately leads to the reduction in evaporation efficiency, earlier described and seen in Fig. 1. There, the rate of thermalization was approximated by the average $\gamma_{\text{th}} = \gamma_{\text{coll}} \sum_{i,j} \varepsilon_{ij} / 9$, as expected for evaporation along all three dimensions. The dipoles were assumed aligned along $\Theta = 90^\circ$, and γ_{th} interpolated over several temperatures to solve Eq. (1). Therefore, we

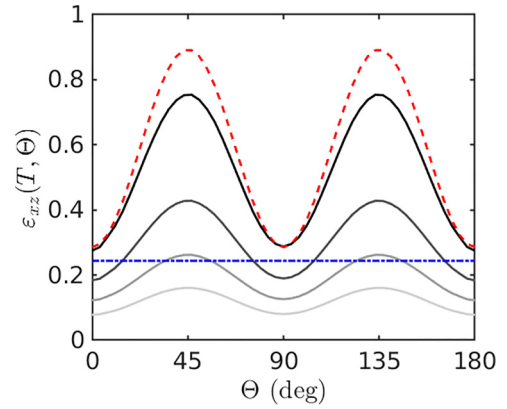


FIG. 4. Plot of ε_{xz} as a function of the dipole tilt angle Θ . The dashed red curve is the analytic threshold ε_{xz} result, whereas the solid curves are those from Monte Carlo integration using the GP interpolated cross sections, at temperatures $T = 10$ nK (black), $T = 100$ nK (dark gray), $T = 400$ nK (gray), and $T = 1$ μ K (light gray). The dashed-dotted blue line is the efficiency for purely p -wave collisions, $\varepsilon_p = 1/4.1$.

recommend that molecular species with larger dipole moments adopt larger microwave detunings during evaporation, reducing their effective dipole moments and taking them close to threshold. Unfortunately, having $\Delta > \Omega$ might lead to higher two-body losses [17], so a fine balance must be struck to both remain close to threshold and maintain low loss rates. Appendix provides a more comprehensive summary of ε_{ij} for all excitation-rethermalization configurations.

Realistically, forced evaporation by trap depth lowering tends to occur primarily along one direction, reducing the evaporation efficiency in the presence of molecular losses [48]. The resulting out-of-equilibrium momentum distribution from single axis evaporation will be much like that in cross-dimensional rethermalization experiments, where an anisotropic collisional efficiency could now be used to ones advantage. For instance, near unity, collisional efficiency is achieved in the threshold regime with ε_{xz} specifically at $\Theta = 45^\circ$. Optimal evaporation protocols could thus be engineered by varying the molecular dipole orientation relative to the axis of evaporation. We leave such investigations to a future work.

Outlook and conclusions. By constructing a GP model of the elastic differential cross section between microwave shielded polar molecular fermions, we have found that non-threshold collisions can greatly diminish the efficacy of collisions toward thermalization of a nondegenerate gas. It is thus prudent to perform evaporation in the threshold regime, with the caveat that Pauli blocking in fermions would also lower the collisional efficiency below the Fermi temperature [21]. If deployed in direct simulation Monte Carlo solvers [27,28,36], this GP model could also permit accurate dynamical studies in the Fermi degenerate or hydrodynamic regimes. The latter is motivated by restrictions of ε_{ij} only being able to describe thermalization in dilute samples. With larger molecular dipoles at densities required to achieve quantum degeneracy, the collision rate is far exceeded by the

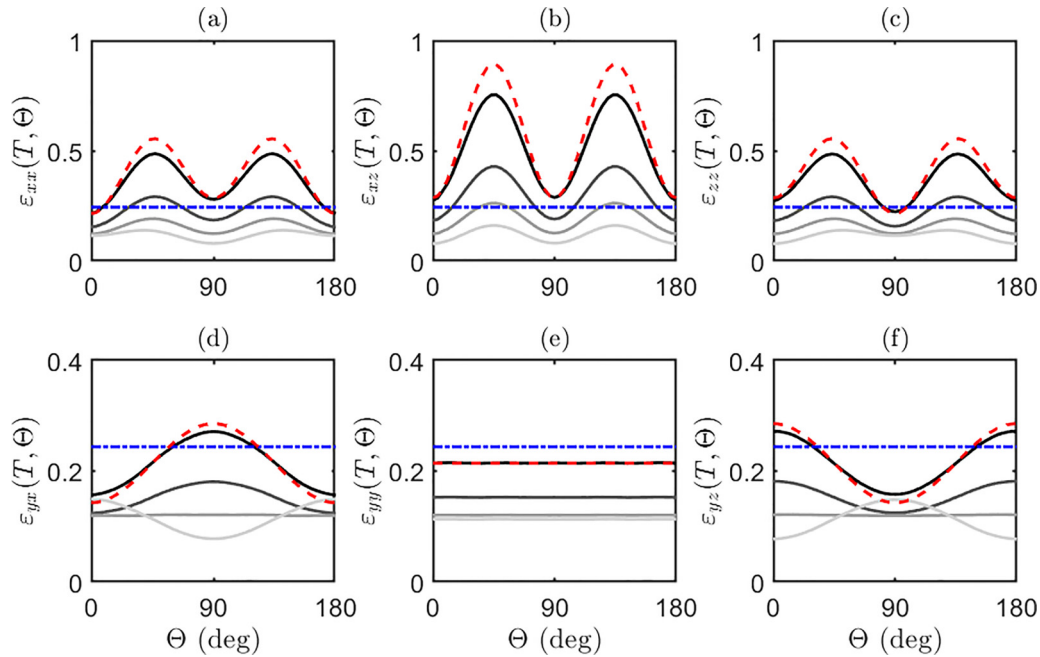


FIG. 5. Plot of ε_{ij} as a function of the dipole tilt angle Θ , for all six unique configurations (a)–(f) of the excitation axis i , and measured thermalization axis j . The subplot formats are consistent with that of Fig. 4 in the main text.

mean trapping frequency, demanding equilibration of trapped dipolar gases be treated within a hydrodynamic framework [49–52]. The method of GP interpolation proposed here could similarly be applied to DC field shielded molecules [53], different microwave polarizations, and bosonic species.

Recently, Bose-Einstein condensation of polar molecules through evaporative cooling was achieved by the Columbia group [54]. There, collisional shielding was performed with a mixture of circular σ^+ -polarized and linear π -polarized microwaves to reduce three-body losses. Although necessary in bosonic species, identical fermions do not scatter in the s -wave channel, allowing a single circularly polarized microwave source to suffice for efficient evaporation [17]. Nevertheless, the GP techniques presented here are, in principle, able to handle elastic differential scattering for arbitrary scatterers, so long as close-coupling calculations can be performed to generate a sufficient data set for training.

Acknowledgments. The authors are grateful to L. Xin-Yu for motivating discussions and insights on evaporation in molecular Fermi gases. This work is supported by the National Science Foundation under Grant No. PHY2110327.

Appendix: Various configurations of the collisional efficiency. In this Appendix, we plot the collisional efficiency for all six unique excitation-rethermalization configurations in Fig. 5. Similar to the format of Fig. 4, each subplot [Figs. 5(a)–5(f)] shows a different (i, j) configuration, within which, ε_{ij} is plotted against the dipole tilt angle Θ as dashed curves, for the temperatures $T = 10$ nK (black), $T = 100$ nK (dark gray), $T = 400$ nK (gray), and $T = 1$ μ K (light gray). The analytic threshold results are also plotted as red-dashed curves in every subplot [28], along with the collision efficiency for purely p -wave scattering (dotted-dashed blue curves) [55].

The collisional efficiency for ε_{yy} is completely independent of Θ , expected from the symmetry imposed by taking $\hat{\mathcal{E}}$ to lie within the x, z plane. Interestingly, we also find that the ε_{ij} terms with only one of the excitation or rethermalization axes lying along y essentially lose their dependence on Θ around 400 nK. Above this temperature, collisional thermalization in these configurations are always less efficient than even nondipolar p -wave scattering for all Θ .

[1] D. DeMille, Quantum computation with trapped polar molecules, *Phys. Rev. Lett.* **88**, 067901 (2002).
 [2] L. D. Carr, D. DeMille, R. V. Krems, and J. Ye, Cold and ultracold molecules: Science, technology and applications, *New J. Phys.* **11**, 055049 (2009).
 [3] D. S. Jin and J. Ye, Introduction to ultracold molecules: New frontiers in quantum and chemical physics, *Chem. Rev.* **112**, 4801 (2012).
 [4] G. Quémener and P. S. Julienne, Ultracold molecules under control! *Chem. Rev.* **112**, 4949 (2012).

[5] J. L. Bohn, A. M. Rey, and J. Ye, Cold molecules: Progress in quantum engineering of chemistry and quantum matter, *Science* **357**, 1002 (2017).
 [6] W. Ketterle and N. J. V. Druten, *Evaporative Cooling of Trapped Atoms* (Academic Press, Cambridge, USA, 1996).
 [7] G. Quémener and J. L. Bohn, Shielding $^2\Sigma$ ultracold dipolar molecular collisions with electric fields, *Phys. Rev. A* **93**, 012704 (2016).
 [8] T. Xie, M. Lepers, R. Vexiau, A. Orbán, O. Dulieu, and N. Bouloufa-Maafa, Optical shielding of destructive chemical

- reactions between ultracold ground-state NaRb molecules, *Phys. Rev. Lett.* **125**, 153202 (2020).
- [9] K. Matsuda, L. D. Marco, J.-R. Li, W. G. Tobias, G. Valtolina, G. Quéméner, and J. Ye, Resonant collisional shielding of reactive molecules using electric fields, *Science* **370**, 1324 (2020).
- [10] J.-R. Li, W. G. Tobias, K. Matsuda, C. Miller, G. Valtolina, L. De Marco, R. R. W. Wang, L. Lassablière, G. Quéméner, J. L. Bohn *et al.*, Tuning of dipolar interactions and evaporative cooling in a three-dimensional molecular quantum gas, *Nat. Phys.* **17**, 1144 (2021).
- [11] B. Mukherjee, M. D. Frye, C. R. Le Sueur, M. R. Tarbutt, and J. M. Hutson, Shielding collisions of ultracold CaF molecules with static electric fields, *Phys. Rev. Res.* **5**, 033097 (2023).
- [12] A. V. Gorshkov, P. Rabl, G. Pupillo, A. Micheli, P. Zoller, M. D. Lukin, and H. P. Büchler, Suppression of inelastic collisions between polar molecules with a repulsive shield, *Phys. Rev. Lett.* **101**, 073201 (2008).
- [13] A. V. Avdeenko, Dipolar collisions of ultracold polar molecules in a microwave field, *Phys. Rev. A* **86**, 022707 (2012).
- [14] L. Lassablière and G. Quéméner, Controlling the scattering length of ultracold dipolar molecules, *Phys. Rev. Lett.* **121**, 163402 (2018).
- [15] T. Karman and J. M. Hutson, Microwave shielding of ultracold polar molecules, *Phys. Rev. Lett.* **121**, 163401 (2018).
- [16] L. Anderegg, S. Burchesky, Y. Bao, S. S. Yu, T. Karman, E. Chae, K.-K. Ni, W. Ketterle, and J. M. Doyle, Observation of microwave shielding of ultracold molecules, *Science* **373**, 779 (2021).
- [17] A. Schindewolf, R. Bause, X.-Y. Chen, M. Duda, T. Karman, I. Bloch, and X.-Y. Luo, Evaporation of microwave-shielded polar molecules to quantum degeneracy, *Nature (London)* **607**, 677 (2022).
- [18] N. Bigagli, C. Warner, W. Yuan, S. Zhang, I. Stevenson, T. Karman, and S. Will, Collisionally stable gas of bosonic dipolar ground-state molecules, *Nat. Phys.* **19**, 1579 (2023).
- [19] J. Lin, G. Chen, M. Jin, Z. Shi, F. Deng, W. Zhang, G. Quéméner, T. Shi, S. Yi, and D. Wang, Microwave shielding of bosonic NaRb molecules, *Phys. Rev. X* **13**, 031032 (2023).
- [20] H. R. Sadeghpour, J. L. Bohn, M. J. Cavagnero, B. D. Esry, I. I. Fabrikant, J. H. Macek, and A. R. P. Rau, Collisions near threshold in atomic and molecular physics, *J. Phys. B: At. Mol. Opt. Phys.* **33**, R93 (2000).
- [21] K. Aikawa, A. Frisch, M. Mark, S. Baier, R. Grimm, J. L. Bohn, D. S. Jin, G. M. Bruun, and F. Ferlaino, Anisotropic relaxation dynamics in a dipolar Fermi gas driven out of equilibrium, *Phys. Rev. Lett.* **113**, 263201 (2014).
- [22] Y. Tang, A. G. Sykes, N. Q. Burdick, J. M. DiSciaccia, D. S. Petrov, and B. L. Lev, Anisotropic expansion of a thermal dipolar Bose gas, *Phys. Rev. Lett.* **117**, 155301 (2016).
- [23] Y. Tang, A. Sykes, N. Q. Burdick, J. L. Bohn, and B. L. Lev, *s*-wave scattering lengths of the strongly dipolar bosons ^{162}Dy and ^{164}Dy , *Phys. Rev. A* **92**, 022703 (2015).
- [24] A. Patscheider, L. Chomaz, G. Natale, D. Petter, M. J. Mark, S. Baier, B. Yang, R. R. W. Wang, J. L. Bohn, and F. Ferlaino, Determination of the scattering length of erbium atoms, *Phys. Rev. A* **105**, 063307 (2022).
- [25] J. L. Bohn, M. Cavagnero, and C. Ticknor, Quasi-universal dipolar scattering in cold and ultracold gases, *New J. Phys.* **11**, 055039 (2009).
- [26] J. L. Bohn and D. S. Jin, Differential scattering and rethermalization in ultracold dipolar gases, *Phys. Rev. A* **89**, 022702 (2014).
- [27] A. G. Sykes and J. L. Bohn, Nonequilibrium dynamics of an ultracold dipolar gas, *Phys. Rev. A* **91**, 013625 (2015).
- [28] R. R. W. Wang and J. L. Bohn, Anisotropic thermalization of dilute dipolar gases, *Phys. Rev. A* **103**, 063320 (2021).
- [29] O. J. Luiten, M. W. Reynolds, and J. T. M. Walraven, Kinetic theory of the evaporative cooling of a trapped gas, *Phys. Rev. A* **53**, 381 (1996).
- [30] K. B. Davis, M.-O. Mewes, and W. Ketterle, An analytical model for evaporative cooling of atoms, *Appl. Phys. B* **60**, 155 (1995).
- [31] F. Deng, X.-Y. Chen, X.-Y. Luo, W. Zhang, S. Yi, and T. Shi, Effective potential and superfluidity of microwave-shielded polar molecules, *Phys. Rev. Lett.* **130**, 183001 (2023).
- [32] X.-Y. Chen, A. Schindewolf, S. Eppelt, R. Bause, M. Duda, S. Biswas, T. Karman, T. Hilker, I. Bloch, and X.-Y. Luo, Field-linked resonances of polar molecules, *Nature (London)* **614**, 59 (2023).
- [33] G. Wang and G. Quéméner, Tuning ultracold collisions of excited rotational dipolar molecules, *New J. Phys.* **17**, 035015 (2015).
- [34] See Supplemental Material at <http://link.aps.org/supplemental/10.1103/PhysRevResearch.6.L022033> for details on the close-coupling calculations, frame transformations for Gaussian process regression, and a derivation of the Eikonal approximation and collision efficiency.
- [35] L. P. Pitaevskii, E. M. Lifshitz, and J. B. Sykes, *Physical Kinetics*, Course of Theoretical Physics (Elsevier Science, Tarrytown, New York, 2017).
- [36] G. A. Bird, Direct simulation and the Boltzmann equation, *Phys. Fluids* **13**, 2676 (1970).
- [37] The differential cross section suffers innate convergence issues due to singularities in the scattering amplitude [26]. Fortunately for us, forward scattering does not contribute to cross-dimensional thermalization, of which we are concerned with in this Letter. We leave addressing these issues to a future paper.
- [38] J. Sacks, S. B. Schiller, and W. J. Welch, Designs for computer experiments, *Technometrics* **31**, 41 (1989).
- [39] J. Cui and R. V. Krems, Efficient non-parametric fitting of potential energy surfaces for polyatomic molecules with gaussian processes, *J. Phys. B: At. Mol. Opt. Phys.* **49**, 224001 (2016).
- [40] A. Christianen, T. Karman, R. A. Vargas-Hernández, G. C. Groenenboom, and R. V. Krems, Six-dimensional potential energy surface for NaKNaK collisions: Gaussian process representation with correct asymptotic form, *J. Chem. Phys.* **150**, 064106 (2019).
- [41] In the dipole frame, the differential cross section has scattering angles obey the symmetry relation $\mathcal{D}_{\text{el}}(E, \eta, \theta_s, \phi_s) = \mathcal{D}_{\text{el}}(E, \eta, \theta_s, -\phi_s)$. Consequently, we only need to specify the differential cross section for angles within the domain $\eta, \theta_s, \phi_s \in [0, \pi]$, to fully describe its global structure.
- [42] C. E. Rasmussen and C. K. I. Williams, *Gaussian Processes for Machine Learning* (The MIT Press, Cambridge, Massachusetts, 2005).
- [43] The Matérn- $\frac{5}{2}$ kernel contains a parameter w that sets a length scale over which features of the data vary in coordinate space, which is optimized during the model training process.

- [44] We utilize more points than usually necessary for GP fitting in this study, so as to obtain more accurate results of subsequently computed quantities in this Letter. We also optimize the model's hyperparameters [56] on top of just the kernel parameters. Even so, the Gaussian process model has issues faithfully reproducing the differential cross section around $\eta, \theta_s = 90^\circ$, known to have a discontinuity at threshold [26]. Fortunately, this angular segment corresponds to forward scattering, which does not contribute to the cross-dimensional thermalization process of interest here. We ignore this issue until necessary for consideration in future works.
- [45] C. R. Monroe, E. A. Cornell, C. A. Sackett, C. J. Myatt, and C. E. Wieman, Measurement of Cs-Cs elastic scattering at $T = 30 \mu\text{K}$, *Phys. Rev. Lett.* **70**, 414 (1993).
- [46] D. W. Snoke and J. P. Wolfe, Population dynamics of a Bose gas near saturation, *Phys. Rev. B* **39**, 4030 (1989).
- [47] The Monte Carlo integration gives a $\lesssim 1\%$ error, which is mostly imperceptible in the log-linear plot.
- [48] E. L. Surkov, J. T. M. Walraven, and G. V. Shlyapnikov, Collisionless motion and evaporative cooling of atoms in magnetic traps, *Phys. Rev. A* **53**, 3403 (1996).
- [49] R. R. W. Wang and J. L. Bohn, Thermal conductivity of an ultracold paramagnetic Bose gas, *Phys. Rev. A* **106**, 023319 (2022).
- [50] R. R. W. Wang and J. L. Bohn, Thermoviscous hydrodynamics in nondegenerate dipolar Bose gases, *Phys. Rev. A* **106**, 053307 (2022).
- [51] R. R. W. Wang and J. L. Bohn, Anisotropic acoustics in dipolar Fermi gases, *Phys. Rev. A* **107**, 033321 (2023).
- [52] R. R. W. Wang and J. L. Bohn, Viscous dynamics of a quenched trapped dipolar Fermi gas, *Phys. Rev. A* **108**, 013322 (2023).
- [53] L. Lassablière and G. Quéméner, Model for two-body collisions between ultracold dipolar molecules around a Förster resonance in an electric field, *Phys. Rev. A* **106**, 033311 (2022).
- [54] N. Bigagli, W. Yuan, S. Zhang, B. Bulatovic, T. Karman, I. Stevenson, and S. Will, Observation of Bose-Einstein condensation of dipolar molecules, [arXiv:2312.10965](https://arxiv.org/abs/2312.10965).
- [55] B. DeMarco, J. L. Bohn, J. P. Burke, M. Holland, and D. S. Jin, Measurement of p -wave threshold law using evaporatively cooled fermionic atoms, *Phys. Rev. Lett.* **82**, 4208 (1999).
- [56] L. Yang and A. Shami, On hyperparameter optimization of machine learning algorithms: Theory and practice, *Neurocomputing* **415**, 295 (2020).